Experimental and Computational Study of Hydration Reactions of Aluminum Oxide Anion Clusters

Jill R. Scott,* Gary S. Groenewold,* Anita K. Gianotto, and Michael T. Benson

Idaho National Engineering and Environmental Laboratory, Idaho Falls, ID 83415

J. B. Wright

Battelle Memorial Institute, 2012 Tollgate Road, Suite 206, Bel Air, Maryland 21015

Received: December 17, 1999; In Final Form: March 12, 2000

Hydration of aluminum oxide anion clusters was studied in the gas phase using an ion trap secondary ion mass spectrometer. Hydration of both AlO_2^- and $Al_2O_4H^-$ occurred by the consecutive addition of two H_2O molecules. For hydration of AlO_2^-, the rate constants for addition of the first and second water molecules are 4×10^{-11} and 4×10^{-10} cm^3 molecule^{-1} s^{-1}, respectively. The first and second hydration rate constants for $Al_2O_4H^-$ are 2×10^{-9} and 8×10^{-10} cm^3 molecule^{-1} s^{-1}, respectively. A comparison of the experimental rate constants to the theoretical rate constants reveals that addition of the first H_2O to AlO_2^- is only 2% efficient, whereas addition of the first H_2O to $Al_2O_4H^-$ is 100% efficient. Ab initio calculations were performed to assist in the interpretation of the kinetic results. Reaction mechanisms and energetics for the hydration of the AlO_2^- system were calculated using the HF/6-311+G(d(Al),p), B3LYP/6-31+G(d), B3LYP/6-311+G(2d,p), B3LYP/6-311+G(3d2f,2p), and MP2/6-311+G(2d,p) levels of theory. Calculations on the hydration of the $Al_2O_4H^-$ system were performed using the B3LYP/6-311+G(2d,p) level of theory. Ab initio results revealed that the addition of the first and second waters, for both the AlO_2^- and $Al_2O_4H^-$ systems, results in the formation of four-membered transition states, with simultaneous Al−O bond formation and proton transfer. However, a significant later transition state is observed, with respect to the Al−O and H−O bond lengths, for the addition of the second water molecule in the $Al_2O_4H^-$ system. A comparison of the reaction mechanisms and energetics was not sufficient to account for the 2 orders of magnitude difference in rate constants; however, the reactivity differences do correlate with the dipole moment of the aluminum oxide anions, which may serve to preorient the incoming water molecule, thus enhancing the reaction rate.

I. Introduction

Metal oxide surfaces have received considerable interest because they are involved in a variety of industrial and natural phenomena. For example, metal oxides are used commercially as catalysts, catalyst supports, ceramic materials, solid phases in chromatography, absorbents, and desiccants. Metal oxides also play a role in microelectronics, optics, and corrosion resistance. In nature, metal oxides, such as silica and alumina, are major constituents of soils and airborne dust particles. As components of geological subsurfaces, metal oxides affect retention, mobilization, and degradation of contaminants. Although there is a need to understand metal oxide surfaces, they are difficult to study[1] because the surface characteristics are often different from the bulk[2] and the surfaces may be composed of multiple sites that have different properties and reactivities. To address the experimental limitations, there has been an increase in theoretical modeling of metal oxide surface structures and reactivity.[3−6] Because of time and cost constraints, the simulation of large surface areas is prohibitive. Therefore, a variety of theoretical modeling methods have been developed. In many theoretical surface models, part of the surface is meticulously modeled while the surrounding area is estimated. In essence, a small cluster is modeled with quantum mechanics and then embedded into a crystal lattice potential[7] to approach a more realistic surface model.

As a logical extension, metal oxide clusters[8−11] have received increased experimental attention over the past decade. Most of these studies are performed in the gas phase because some gas-phase techniques offer the advantage of being able to select and isolate reactants as well as monitor reaction products.[12] Two of the major motivations for studying clusters in the gas phase are (1) that clusters serve as simplified models of bulk surfaces and (2) that clusters can be considered as novel nanophase materials with properties distinct from the bulk. At first glance, these motivations appear to be diametrically opposed to each other. However, clusters can be formed over a wide range of sizes, which span the gap between the gas phase and the condensed phase. The size at which a particular type of cluster may switch from having distinct molecular properties to having properties resembling bulk characteristics depends on the material.[13,14] For example, similarities between reactions of gas-phase metal oxides to reactions of surface catalysts have been observed for metal oxide species such as $Mo_xO_y^+$ ($x = 1-3$)[15] and $Nb_xO_y^+$ ($x = 3-5$).[16] Although most metal oxide studies have focused on cation species, anion clusters would more accurately reflect many natural mineral surfaces as they are predominantly negatively charged because of insufficient bonds to compensate for surface oxygen atoms.[17] The surface sites of

* Corresponding authors. Address: 2525 N. Fremont Ave., MS 2208, Idaho Falls, ID 83415. Phone: (208) 526-2803. Fax: (208) 526-8541. E-mail: scotjr@inel.gov and gsg@inel.gov.

10.1021/jp9944435 CCC: $19.00
Published on Web 07/12/2000

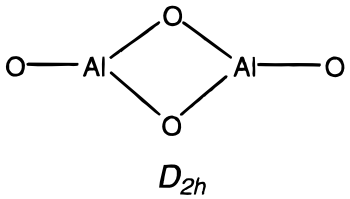

Figure 1. Predicted rhombic-like structure of $A1_2O_4$ (D_{2h} symmetry).

some minerals, such as crytallite edges in smectites, exhibit properties that correspond closely to those of their analogous Si and Al oxides.[18] Therefore, aluminum oxide anion clusters are good candidates for studies aimed at comparing gas-phase cluster reactivity with that observed on bulk surfaces.

Aluminum oxide clusters have been studied both experimentally and theoretically. The simplest aluminum oxide cluster, AlO, has been formed in the gas phase by various methods.[19−23] Zenouda et al.[24] have calculated the electronic states of both AlO and AlO^- to predict the photoelectron spectrum. For neutral AlO_2 species, both linear and cyclic structures have been identified in matrix isolation experiments.[25−27] Larger clusters (Al_xO_y, $x = 2, 3$) have produced a wider variety of structures.[26−29] In 1992, Nemukhin and Weinhold[30] published a paper that serves as a good review because they extensively compared their results, using natural bond orbital analysis, with previous experimental and theoretical work of others. Recent theoretical and photoelectron spectroscopy results tend to view Al_2O_y clusters (both neutral and anionic) as having rhombic-like structures,[26,28,31] with D_{2h} symmetry, in which two oxygen atoms each form a bridge between two Al atoms, as illustrated in Figure 1. However, it should be noted that evidence for such structures has not been produced in matrix isolation experiments.[25] If aluminum oxide anion clusters do have rhombic-like structures, then they should mimic bulk reactivity, as the bulk also contains rhombic-like structures.[32] Whereas the gas-phase structures have been investigated, reactions of aluminum oxide clusters with adsorbates, even simple H_2O, have not been studied.

In contrast to the reactions of the clusters, the hydration of aluminum oxide surfaces has been explored both theoretically and experimentally. The adsorption of water on alumina surfaces is complex, as it involves chemisorption, quasichemisorption, physisorption, and capillary condensation.[33] McHale et al.[34] estimated that, in their experiments, about 33% of absorbed water was chemisorbed. To interpret macroscopic experiments,[33,35,36] researchers have postulated that water is first hydrogen bonded to an alumina surface. The positive Al sites then act as Lewis acids in attracting the water oxygen atom, whereas the negative O site acts as a Lewis base in attracting a water hydrogen, dissociating H_2O, and leading to the formation of −OH and −H groups covalently bound to the surface. This view is consistent with an ionic view of the α-Al_2O_3 surface in which Al^{3+} has transferred electrons to O^{2-}. From ab initio calculations, Salasco et al.[5] suggest that Al will lose 60% of its valence electrons to O. Coustet and Jupille[37] have used high-resolution electron-energy-loss spectroscopy to investigate the adsorption of H_2O on alumina surfaces. Although they could not definitively determine the nature of the site where H_2O dissociation occurs, their results would be consistent with the common assertion that it is a coordinatively unsaturated Lewis site.[38,39] George and co-workers[40] utilized temperature-programmed desorption (TPD) to monitor isotopic exchange reactions of $H_2{}^{18}O$ with Al_2O_3 surface to determine that H_2O adsorption is dissociative. Nelson et al.[41] have used laser-induced thermal desorption and TPD to study the desorption of H_2O from a single-crystal α-Al_2O_3(0001) surface. Because the desorption of H_2O occurred over a broad temperature range from 300 to 500 K, they concluded that there are a variety of hydroxyl surface sites that have different binding energies ranging from 23 to 41 kcal/mol. Wittbrodt et al.[32] have studied the interaction of a theoretical model of the α-aluminum oxide surface with water. In these studies, they modeled molecular physisorption and dissociative adsorption mechanisms and concluded that it is energetically favorable for molecularly adsorbed water to undergo dissociative adsorption. They also attempted to estimate the kinetics of hydration. However, depending on the model used, they could only estimate that hydration could be as slow as 1×10^{-2} s or as fast as 5×10^{-12} s. Because the hydration of aluminum oxide surfaces is complex, it is difficult to determine parameters such as the rate of dissociative adsorption of H_2O on the surface.

To circumvent the complexity of multiple surface hydration reactions, the focus of this paper is on hydration reactions of aluminum oxide anion clusters in the gas phase. Experimental studies were conducted using an ion trap secondary ion mass spectrometer (IT-SIMS). Al_xO_y clusters were generated by bombarding alumina samples with a ReO_4^- primary ion beam, which has the capability of efficiently producing anions from the top surface monolayer. The anions were then stored in the ion trap, where the species of interest could be selected and subsequently reacted with water vapor. The kinetics of the condensation reactions leading to the hydrated species $AlO_2(H_2O)_2^-$ and $Al_2O_4H(H_2O)_2^-$ were investigated. Insights into the structure of cluster species and reaction mechanisms were obtained through ab initio calculations and elimination reactions.

II. Experimental Section

Samples. Alumina (Brockman I, neutral) was obtained from Aldrich (Milwaukee, WI). Untreated alumina was used for condensation experiments involving m/z 59. Because the abundance of m/z 119 ions produced from untreated alumina was not sufficient for well-defined ion−molecule experiments, these experiments were performed using Cs^+-treated alumina. Investigations into the mechanism responsible for enhancement of ion abundances due to Cs^+ treatment are currently being pursued. Powdered samples were attached to the end of a 2.7-mm probe tip with double-sided tape (3M, St. Paul, MN).

Cs^+-treated alumina was produced by the following steps. (1) Approximately 1 g of alumina was placed into a 150 mL beaker to which 30 mL of Nanopure (NP) water was added. The mixture was stirred to form a slurry with a Teflon-coated stir bar. (2) While the slurry was stirred, 10 mL of 0.44 M $CsNO_3$ (99.99% pure, obtained from Aldrich, Milwaukee, WI) was added in a dropwise fashion. (3) After the addition of the $CsNO_3$ solution, the slurry was stirred for a minimum of 24 h. (4) The slurry was then centrifuged, and the supernatant discarded. (5) The residue was washed three times with 15 mL of NP H_2O. (6) Then, 25 mL of NP H_2O was added to the residue. (7) Steps 2−6 were repeated three times. 8) After the final exchange, the washed mixture was transferred to a clean Petri dish, covered, and placed in a vacuum oven at 100 °C for 12 h.

Instrumentation. The IT-SIMS instrument utilized in these studies has been described previously.[42−46] Briefly, this IT-SIMS setup is a modified Finnigan ITMS instrument (Finnigan Corp., San Jose, CA). Modifications include the incorporation of a perrhenate (ReO_4^-) primary ion beam,[44] an insertion lock for the introduction of solid samples, and an offset dynode with a

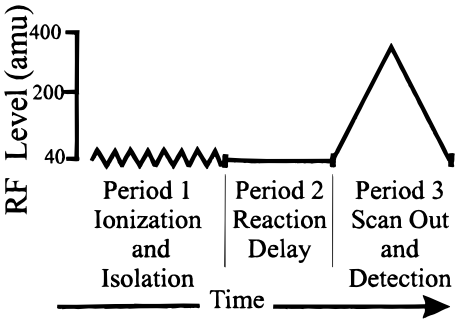

Figure 2. Experimental sequence of events for MS^2 condensation reactions. In Period 1, saw-toothed line represents application of FNF for ion isolation.

multichannel plate detector. The primary ion gun and sample probe tip are collinear and located outside opposite end caps of the ion trap. The primary ion gun was operated at 4.5 keV and produced a 95-pA ReO_4^- beam with a 1.25-mm diameter. A ReO_4^- beam was used because this type of ion beam is more efficient for sputtering intact surface species into the gas phase than atomic particle bombardment.[44,45,46] The data acquisition and control system uses Teledyne Apogee ITMS Beta Build 18 software that controls routine ITMS functions and a Teledyne HST-1000 filtered-noise field (FNF) system (Teledyne Electronic Technologies, Mountain View, CA). Data analysis was performed using SATURN 2000 software (version 1.4, Varian, Walnut Creek, CA).

For MS^2 experiments, water vapor was added via a variable leak valve up to pressures of 5×10^{-6} Torr. Ion gauge pressures are reported uncorrected because response to H_2O is nearly identical to that of nitrogen.[47] Helium bath gas was added to reach an operating pressure of 3×10^{-5} Torr (uncorrected). The IT-SIMS base pressure was 3×10^{-8} Torr.

IT-SIMS Parameters. For typical MS experiments, the ion trap was operated with a low-mass cutoff of 40 amu, which corresponds to $a_z = 0$, $q_z = 0.9078$, and $\beta = 0.9802$. Ionization times varied from 40 to 160 ms. Ions were then detected using a mass-selective instability scan with axial modulation.[48] Background spectra were collected after each sample to account for any signal originating from grids on the ion trap end caps. Seven spectra (each composed of the average of 15 or 20 scans) were averaged and background-corrected to obtain final peak intensities. The relative standard deviation between averaged spectra was ±5%. All spectra were acquired in the negative mode.

A typical sequence of events for ion−molecule condensation experiments is illustrated in Figure 2. Parameters for condensation experiments are similar to those for the MS studies with a few exceptions. Ionization times to produce sufficient ions for condensation experiments varied from 40 to 80 ms for the production of *m*/*z* 119 and 59, respectively. Ion isolation occurred simultaneously with the ionization event. Ions of interest were isolated by applying a "notched" filtered-noise field (FNF), as illustrated in Figure 2. In this method, a broadband of radio frequencies, except for a "notch" at those frequencies that correspond to the mass being isolated, is applied to eject unwanted ions. The delay time between the ionization/isolation event and the detection event was varied to allow the isolated ions to react with water molecules. Ions were then detected and final spectra obtained in the same manner as for the MS experiments.

Collision-induced dissociation (CID) reactions were performed on the hydrated species in an attempt to determine if the hydrated species could be dissociated. As in the condensation experiments, the ionization and isolation events occurred simultaneously in these MS^2 experiments. After isolation, the ions of interest were collisionally activated by the application of an axial RF pulse at the natural frequency of the isolated ions. The RF pulse was applied for various combinations of time and amplitude ranging from 10 to 500 ms and 0.2 to 7.0 V_{p-p} to achieve dissociation and trapping of fragment ions. Ions present in the trap were then scanned out and detected.

Computational Methods. Initial computations on the anions were performed using the General Atomic and Molecular Electronic Structure System (GAMESS)[49] program at the Hartree−Fock (HF) level of theory. The HF calculations utilized the 6-311G basis set with a diffuse sp shell added to O and Al, a d-type polarization function added only to Al, and a p-type polarization function added to H [denoted as HF/6-311+G(d(Al),p)]. Frequency calculations were performed on all minima to determine the mode of vibration. Intrinsic Reaction Coordinate (IRC) calculations[53,54] were performed on all transition states at the HF/6-311+G(d(Al),p) level of theory to ensure that the reactants, transition states, and products occurred on the same reaction path. To include correlation contributions, single-point energies were calculated with the Møller−Plesset second-order perturbation theory (MP2)[55,56] using the HF/6-311+G(d(Al),p)-optimized geometries and are denoted as MP2/6-311+G(d(Al),p)//HF/6-311+G(d(Al),p). Energies were corrected using the zero-point energies from the HF/6-311+G(d(Al),p) calculations.

To further investigate the anionic systems, ab initio molecular orbital calculations were performed using the Gaussian 98 program.[57] In the AlO_2^- system, all structures were fully optimized using the B3LYP exchange and correlation functionals[58,59] with the 6-31+G(d), 6-311+G(2d,p), and 6-311+G(3d2f,2p) basis sets and using the Møller−Plesset perturbation theory[55,56] with the 6-311+G(2d,p) basis set. These levels of theory were investigated to find the optimal level of theory for these systems. A comparison of the geometries and energetics determined at all four levels of theory showed that B3LYP/6-311+G(2d,p) gave results very similar to the MP2/6-311+G(2d,p) level of theory. Therefore, for the larger $Al_2O_4H^-$ system, calculations were only performed using the B3LYP/6-311+G(2d,p) level of theory. All minimizations were carried out using the Berny algorithm,[60,61] and the default parameters were used for the integral cutoff and minimization convergence criteria. Vibrational frequencies were calculated for all minima at all levels of theory to obtain the zero-point energy and to ensure that the transition states had only one imaginary frequency and that all other minima had zero imaginary frequencies.

III. Results and Discussion

A typical anion IT-SIMS spectrum of aluminum oxide is shown in Figure 3a. The dominant peaks in the spectrum are at *m*/*z* 43, 59, 95, 155, and 179, which correspond to the elemental compositions AlO^-, AlO_2^-, $AlO_4H_4^-$, $Al_2O_6H_5^-$, and $Al_3O_6H_2^-$, respectively. This spectrum was acquired immediately after the sample was inserted into the vacuum chamber, which was operating with a He bath gas pressure of 3×10^{-5} Torr (no water vapor added). For samples analyzed immediately after insertion, the dihydrated species at *m*/*z* 95, $AlO_2(H_2O)_2^-$, is more abundant than either the dehydrated species at *m*/*z* 59, AlO_2^-, or the monohydrate species at *m*/*z* 77, $AlO_2(H_2O)^-$. Additionally, the dihydrated dimer species at *m*/*z* 155, $Al_2O_4H(H_2O)_2^-$, is also present, whereas the dehydrated and monohydrated dimer species are either not observed or observed at low abundances. When alumina samples were analyzed after prolonged exposure

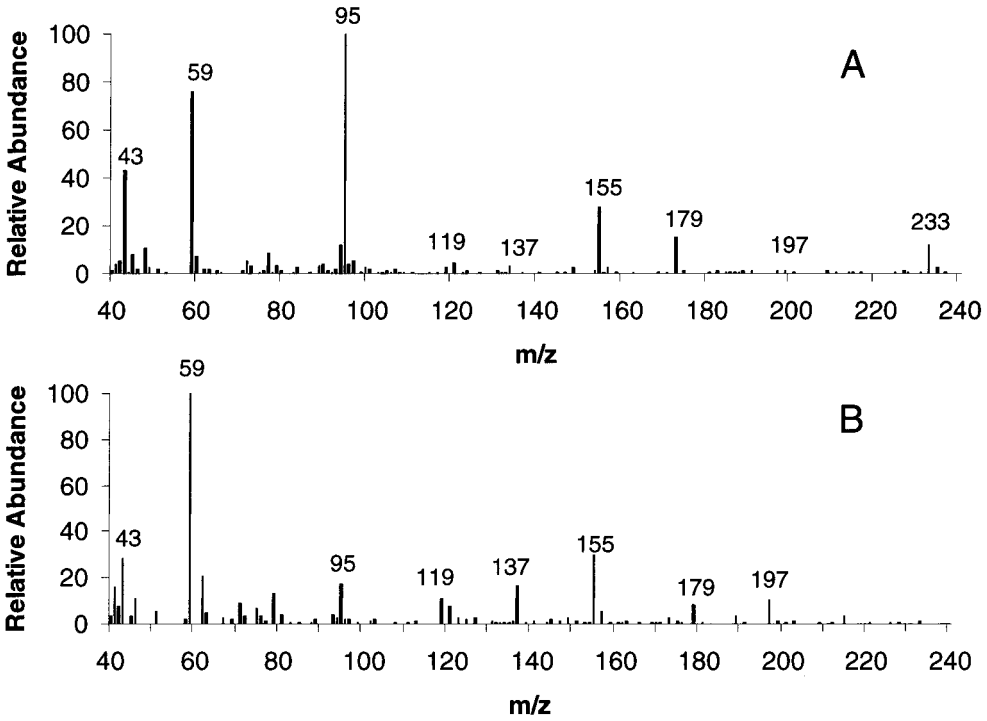

Figure 3. Anion IT-SIMS spectra of aluminum oxide sample acquired (A) immediately after insertion at 3×10^{-5} torr and (B) after exposure to 8×10^{-8} torr for 12 h.

to high vacuum (8×10^{-8} Torr for 12 h), *m*/*z* 59 was the dominant peak, and the abundance of *m*/*z* 95 was greatly reduced (Figure 3b). The relative abundance of three additional peaks, at *m*/*z* 119, 137, and 197, also increased significantly. The assigned compositions of these peaks are $Al_2O_4H^-$, $Al_2O_5H_3^-$, and $Al_3O_7H_4^-$, respectively. The appearance of spectra from alumina samples analyzed after exposure to low pressure (10^{-8} Torr) in the IT-SIMS for several hours (Figure 3b) are significantly different from spectra from samples analyzed immediately after insertion (Figure 3a). A reasonable explanation for the differences is that some water molecules are initially physisorbed on the aluminum oxide surface. This observation is consistent with the estimate, made by McHale et al.,[34] that approximately 66% of absorbed water is physisorbed.

As ions and H_2O are sputtered into the gas phase from fresh samples, ion−molecule reactions occur, producing the majority of the dihydrated species. This is corroborated by lifetime studies. In these studies, the sample is exposed to the ReO_4^- beam for extended periods of time (several hours). The relative abundance of hydrated species decreases with increased beam exposure. This phenomenon is interpreted to mean that, over time, the ReO_4^- beam sputters away the top monolayer of the sample, which includes physisorbed H_2O. Although the abundance of the peaks corresponding to the hydrated species is reduced with prolonged exposure to the ReO_4^- beam, these peaks are not totally eliminated. Also, longer exposure of samples to low pressure does not completely eliminate evidence of hydrated species, as the spectra are not significantly different in appearance from the spectra in Figure 2b. These observations are consistent with the view that the first monolayer of H_2O is irreversibly chemisorbed, whereas additional layers are reversibly physisorbed on the alumina surface.[33]

Large oligomer species with the general formula $(AlO_2)_x H_{x-1}(H_2O)_y^-$ are observed up to *m*/*z* 593, which corresponds to the trihydrated ($y = 3$) nonamer ($x = 9$). The origin of these species has not yet been established. They may be formed from the surface intact. Alternatively, they may form from condensation reactions in the desorption plume involving neutral alumina species as well as H_2O. Some oligomers may be produced by gas-phase condensation reactions that proceed too rapidly to be studied with the current instrumentation. However, the primary source for the lower-mass oligomers is definitely condensation reactions with H_2O in the gas phase.

The hydration reactions of AlO_2^- and $Al_2O_4H^-$ were studied in detail because they appear to originate from the surface and their condensation reactions occur in the gas phase. These two species are the first in the oligomer series, $AlO_2(AlOOH)_n^-$, that is sputtered into the gas phase even from alumina surfaces exposed to the vacuum environment for prolonged time periods.

AlO_2^- Hydration Kinetics. To understand the kinetics and reactivity of these species, condensation experiments were performed. AlO_2^- (*m*/*z* 59) was isolated in the ion trap and subsequently reacted with a controlled concentration of H_2O vapor at various reaction times. Representative spectra for hydration reactions in the presence of 5×10^{-6} Torr H_2O are shown in Figure 4. At short reaction times (20 ms), most of the AlO_2^- is unreacted, although a tiny amount of the monohydrated species $AlO_3H_2^-$ can also be observed at *m*/*z* 77 (Figure 4a). After a reaction time of 100 ms (Figure 4b), the dihydrated species, $AlO_4H_4^-$, is observed at *m*/*z* 95 with an abundance similar to that of *m*/*z* 59. Again, the abundance of *m*/*z* 77 is very low. With a reaction time of 600 ms (Figure 4c), only *m*/*z* 95 can be observed. In Figure 5a, the reaction progress can be seen in a plot of relative peak abundance versus time. The plot in Figure 5a is consistent with the set of consecutive reactions in eq 1 and eq 2.

$$AlO_2^- + H_2O \xrightarrow{k_1} AlO_3H_2^- \quad (1)$$

$$AlO_3H_2^- + H_2O \xrightarrow{k_2} AlO_4H_4^- \quad (2)$$

Because the abundance of *m*/*z* 77 remains low throughout the

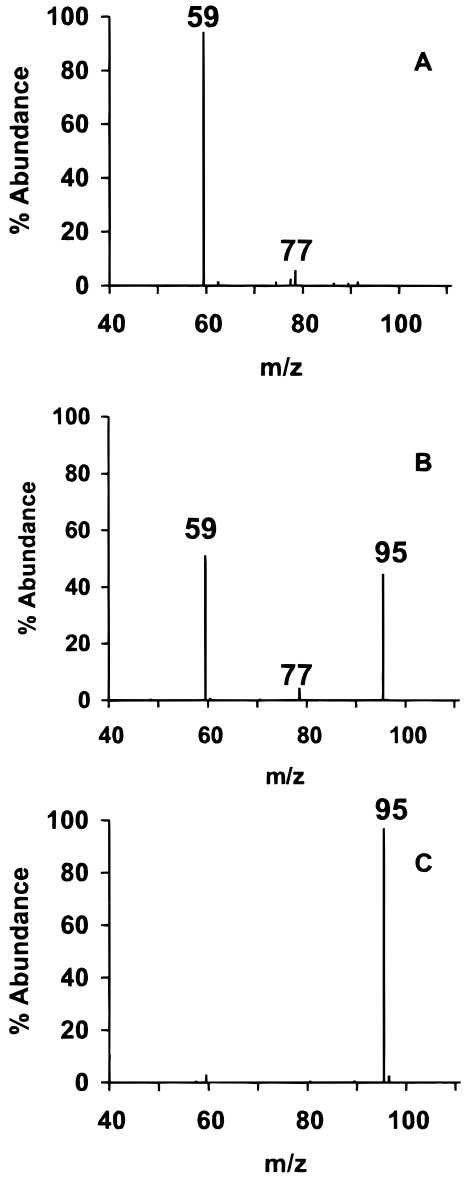

Figure 4. Anion IT-SIMS spectra from condesation reaction of isolated $A1O_2^-$ (*m*/*z* 59) with H_2O pressure of 5×10^{-6} Torr. Reaction times of (A) 0 msec, (B) 100 msec, and (C) 600 msec.

process, the reaction in eq 1 (*m*/*z* 59 → 77) occurs more slowly than the subsequent consecutive reaction in eq 2 (*m*/*z* 77 → 95).

Because the concentration of H_2O is significantly greater than those of the ions produced and therefore remains essentially constant throughout the reaction, these reactions behave with pseudo-first-order kinetics. The experimental rate constant k_1^{exp} was estimated from the rate of disappearance of *m*/*z* 59 to be 3×10^{-11} cm^3 molecule^{-1} s^{-1}. Although the precision of the relative peak abundances between spectra is quite good (relative standard deviation of ±5%), more uncertainty is introduced by the pressure measurement of H_2O. Although the reproducibility of the H_2O pressure is good and the ion gauge response to H_2O is similar to its response to N_2,[50] the absolute accuracy is somewhat uncertain, especially at low pressure. Experiments repeated at other water vapor pressures gave similar rate constants within ±30%, which is probably representative of the uncertainty in the pressure measurement. Therefore, the uncertainty in k_1^{exp} is approximately ±30%.

The theoretical rate constant k_1^{ADO} was calculated to be 2×10^{-9} cm^3 molecule^{-1} s^{-1} using the average-dipole-orientation

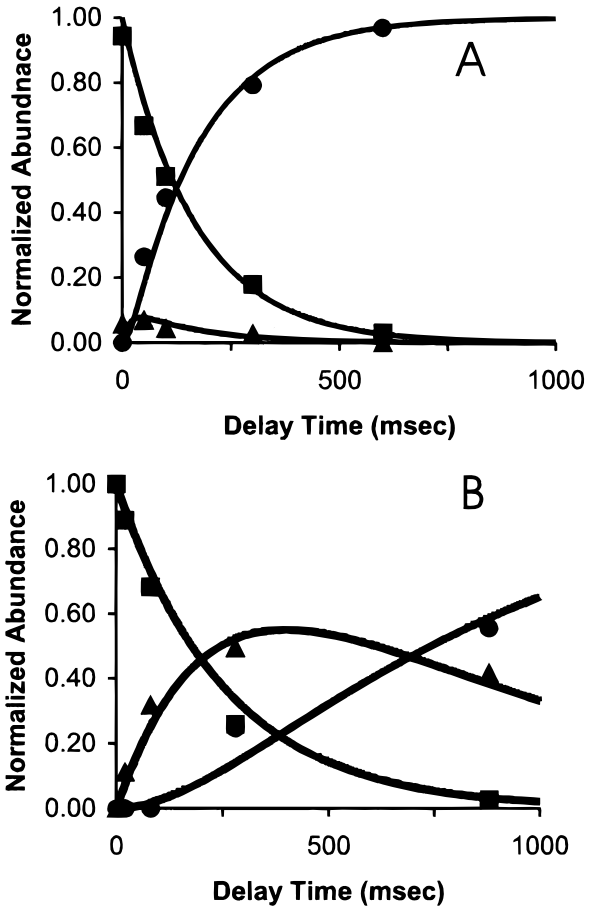

Figure 5. (A) Kinetic reaction plot for $A1O_2^-$ (*m*/*z* 59) condensation reactions with H_2O at a pressure of 5×10^{-6} Torr (estimated $[H_2O] = 1.6 \times 10^{11}$ molecule cm^{-3}). Experimental data are plotted for *m*/*z* 59 (■), *m*/*z* 77 (▲), and *m*/*z* 95 (●). (B) Kinectic reaction plot for $A1_2O_4H^-$ (*m*/*z* 119) condesation reactions with H_2O at a pressure of 6×10^{-8} torr (estimated $[H_2O] = 1.8 \times 10^9$ molecule cm^{-3}). Experimental data are plotted for *m*/*z* 119 (■), *m*/*z* 137 (▲), and *m*/*z* 155 (●). Lines were obtained by fitting the data to theoretical consecutive first-order reaction equations.

(ADO) theory developed by Su and Bowers.[62,63] Parameters were adjusted for the reaction temperature (310 K).[64] A comparison of k_1^{exp} with k_1^{ADO} (Table 1) reveals that the reaction efficiency is only 2%. A confirmation of k_1 and a determination of k_2 were obtained by fitting the data in Figure 5a to the following theoretical equations for consecutive first-order reactions:[65,66]

$$A = A_0 e^{-k_1 t} \tag{3}$$

$$B = B_0 e^{-k_2 t} + \frac{k_1 A_0}{(k_2 - k_1)}(e^{-k_1 t} - e^{-k_2 t}) \tag{4}$$

$$C = C_0 + A_0(1 - e^{-k_1 t}) + B_0\left[1 - e^{-k_2 t} - \frac{A_0/B_0}{1 - k_2/k_1}(e^{-k_2 t} - e^{-k_1 t})\right] \tag{5}$$

The relative abundances of *m*/*z* 59, 77, and 95 were used for *A*, *B*, and *C*, respectively. As seen in Figure 5a, there is good agreement between the experimental data and the theoretical fit. From the theoretical fit, k_1^{Fit} is 4×10^{-11} cm^3 molecule^{-1} s^{-1}, which agrees well with k_1^{exp} (Table 1). The value for k_2^{Fit} is 4×10^{-10} cm^3 molecule^{-1} s^{-1}, which is 10 times faster than k_1, as expected; therefore, the rate-limiting step for hydration of AlO_2^- is addition of the first water, as illustrated in eq 1.

TABLE 1: Experimental and Theoretical Kinetic Rate Constants[a] for Hydration of AlO_2^- and $Al_2O_4H^-$

reaction	k_1^{exp} [b]	k_1^{ADO} [c]	k_1^{Fit} [d]	k^{Fit} [d]	% efficiency[e]
$AlO_2^- + 2H_2O \rightarrow AlO_4H_4^-$	3×10^{-11}	2×10^{-9}	4×10^{-11}	4×10^{-10}	2
$Al_2O_4H^- + 2H_2O \rightarrow Al_2O_6H_5^-$	2×10^{-9}	2×10^{-9}	2×10^{-9}	8×10^{-10}	100

[a] All rate constants given in units of cm^3 molecule^{-1} s^{-1}. [b] Uncertainty of experimental rate constants is ±30%. [c] Theoretical rate constant calculated using average-dipole-orientation theory.[62−64] [d] Rate constants from fit of data to eqs 3−5. [e] Efficiency calculated as k_1^{exp}/k_1^{ADO}.

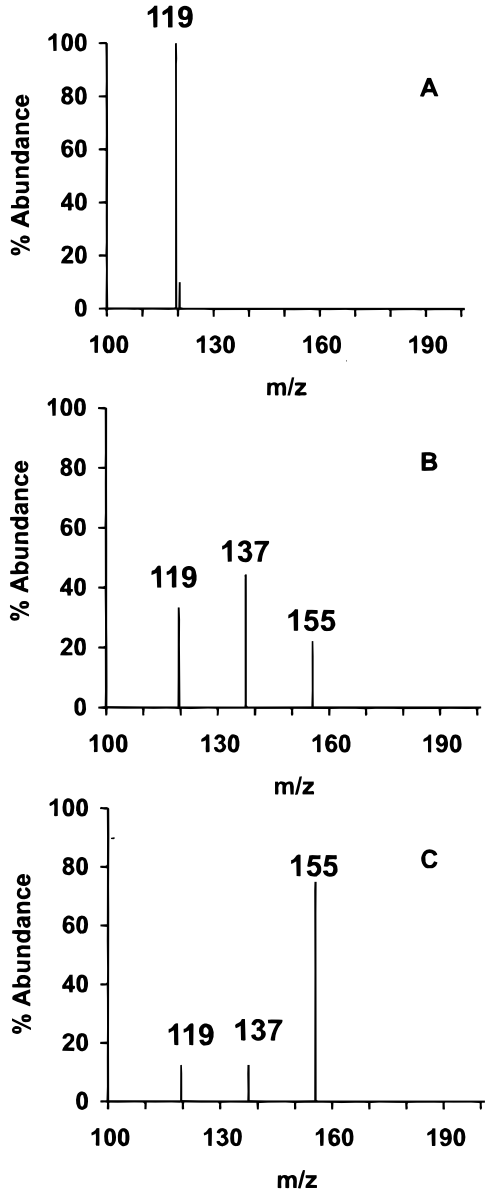

Figure 6. Anion IT-SIMS spectra from condensation reaction of isolated $A1_2O_4H^-$ (*m*/*z* 119) with H_2O at a pressure of 6×10^{-8} Torr. Reaction times of (A) 0 msec, (B) 280 msec, and (C) 1880 msec.

$Al_2O_4H^-$ Hydration Kinetics. Similar condensation experiments were performed to investigate the kinetics and reactivity of hydration of the dimer species, $Al_2O_4H^-$. After isolation of $Al_2O_4H^-$ (*m*/*z* 119), the hydration was allowed to proceed for various reaction times. Typical spectra for various reaction times in the presence of 6×10^{-8} Torr H_2O are shown in Figure 6. The spectrum in Figure 6a was obtained with a 0-ms delay and shows a peak at *m*/*z* 119 that corresponds to the unreacted species $Al_2O_4H^-$. A reaction time of 280 ms (Figure 6b) produces peaks at *m*/*z* 119, 137, and 155 that have approximately equal intensities. These peaks represent the dehydrated species $Al_2O_4H^-$, the monohydrated species $Al_2O_4H(H_2O)^-$, and the dihydrated species $Al_2O_4H(H_2O)_2^-$, respectively. After a 1880-ms reaction time (Figure 6c), the dominant peak in the spectrum is at *m*/*z* 155 ($Al_2O_6H_5^-$). However, a small peak is still present at *m*/*z* 119. Because the IT-SIMS is currently limited to a sequence time of 2 s, these reactions were repeated with higher H_2O pressures up to 1×10^{-7} Torr to determine if the reaction went to completion. In these experiments, there was a residual 10% of the ions contributing to the peak at *m*/*z* 119 that never reacted. It is conceivable that *m*/*z* 119 is composed of more than one ion species. Because of the lack of resolution inherent to the IT-SIMS technique, it is not possible to determine if the species have different elemental compositions or if they are composed of the same elements. Judging from the lack of reactivity, if these species do have the same elemental composition, then they must have different structural characteristics. Different structural isomers are likely considering the variety of isomers suggested for similar Al_2O_y cluster species.[26,28,29] If 10% of the abundance of the peak at *m*/*z* 119, due to unreacted species, is subtracted out, then the reaction does appear to approach completion.

The progress of hydration reactions of $Al_2O_4H^-$, at 1×10^{-8} Torr H_2O pressure, are presented in Figure 5b in a plot of the corrected relative peak abundances versus the reaction time. The reaction plot in Figure 5b is consistent with the set of consecutive reactions in eqs 6 and 7.

$$Al_2O_4H^- + H_2O \xrightarrow{k_1} Al_2O_5H_3^- \quad (6)$$

$$Al_2O_5H_3^- + H_2O \xrightarrow{k_2} Al_2O_6H_5^- \quad (7)$$

Even though the concentration of H_2O in this experiment is 2 orders of magnitude less than that in the AlO_2^- hydration experiment, it is still significantly greater than the concentration of ions. Therefore, the reactions in eqs 6 and 7 follow pseudo-first-order kinetics. From the disappearance of *m*/*z* 119, the experimental rate constant k_1^{exp} was estimated to be 2×10^{-9} cm^3 molecule^{-1} s^{-1}. Rate constant values are summarized in Table 1.

In the same manner that the reaction plot in Figure 5a was fit using eqs 3, 4, and 5 for consecutive first-order reactions, the data in Figure 5b can also be modeled. The relative abundances for *m*/*z* 119 ($Al_2O_4H^-$), *m*/*z* 137 ($Al_2O_5H_3^-$), and *m*/*z* 155 ($Al_2O_6H_5^-$) were substituted for *A*, *B*, and *C*, respectively. As seen in Figure 5b, the agreement between the experimental data and the theoretical fit is quite good. The value for k_1^{Fit} was determined to be 2×10^{-9} cm^3 molecule^{-1} s^{-1}, which is the same as the value for k_1^{exp}. The rate constant k_2^{Fit} was calculated to be 8×10^{-10} cm^3 molecule^{-1} s^{-1}. Unlike for the hydration of AlO_2^-, the rate-limiting step for hydration of $Al_2O_4H^-$ is the second addition of H_2O. For hydration of $Al_2O_4H^-$, k_1^{Fit} is 2.5 times as fast as k_2^{Fit}, which makes observation of the first hydration product, $Al_2O_5H_3^-$, at *m*/*z* 137 easier. A comparison of k_1^{exp} with the theoretical rate constant k_1^{ADO} reveals that the reaction efficiency for addition of the first water to $Al_2O_4H^-$ is 100%. Although the theoretical rate constants, k_1^{ADO}, are the same for hydration of AlO_2^- and $Al_2O_4H^-$, the rate constant k_1^{exp} for the first addition of H_2O to AlO_2^- is only 3×10^{-11} cm^3 molecule^{-1} s^{-1}, which gives a

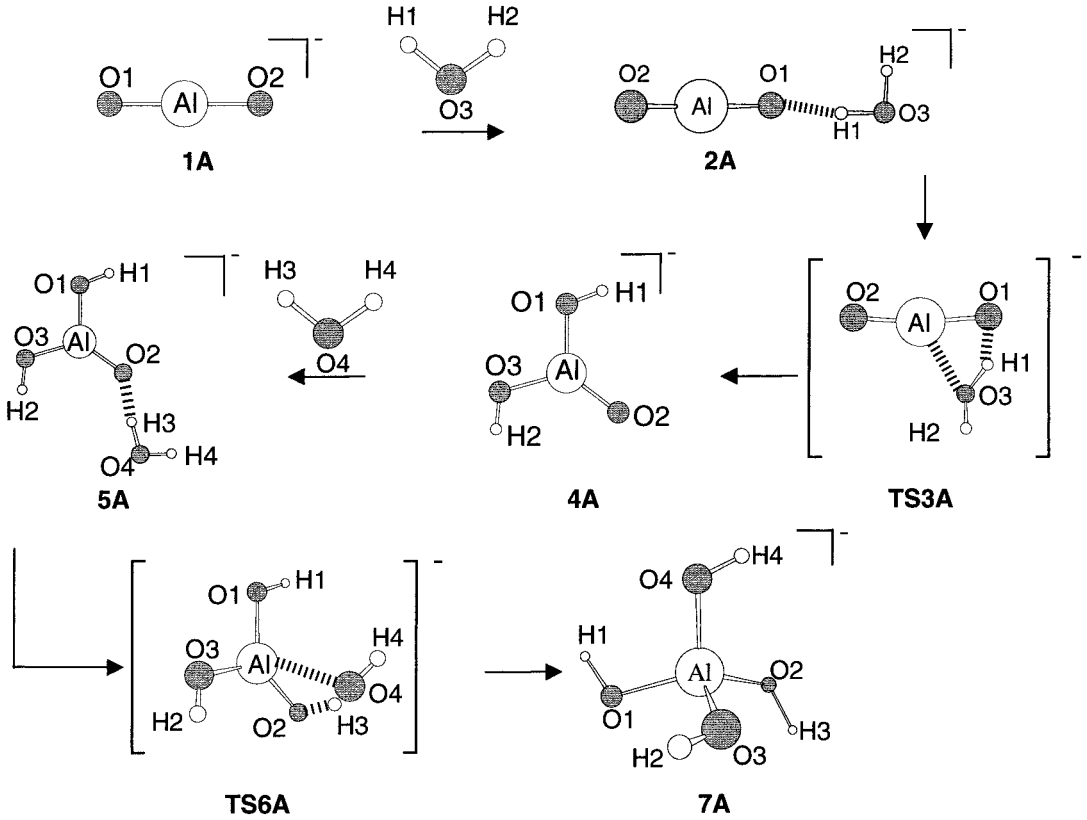

Figure 7. Reaction pathway for hydration of $A1O_2^-$. Structures based on B3LYP/6-311+G(2d,p) level of theory.

reaction efficiency of 2%. Interestingly, the rate constants, k_2^{Fit}, for the second H_2O addition for both AlO_2^- and $Al_2O_4H^-$ are on the order of 10^{-10} cm^3 molecule^{-1} s^{-1}.

Wittbrodt et al.[32] estimated the kinetics for the transition from molecularly to dissociatively absorbed H_2O on aluminum oxide clusters (Al_4O_6 and Al_8O_{12}), both as free clusters and as simulated surfaces. They estimated the rate constants for 300 and 1000 K using transition state theory and Arrhenius parameters. The unimolecular rate constants reported by Wittbrodt et al., for free clusters at 300 K, vary from 4×10^{-4} to 1×10^4 s^{-1}. Interestingly, when they embedded the alumina cluster in a sea of point charges to simulate a surface, the estimated rate for the transition from molecularly to dissociatively absorbed H_2O increased from 10^{-2} to 10^{-12} s. If this trend is valid, then the experimental gas-phase cluster kinetic rates should represent the lower limit for the rate of hydration of an aluminum oxide surface.

Because of the disparity in hydration kinetics, ab initio calculations were performed to address the question: "Is there a difference in the reaction mechanisms or energetics that will explain the different reaction efficiencies?"

$AlO_2^- + 2H_2O \rightarrow AlO_4H_4^-$ Reaction Mechanism. Previous computational methods used to determine aluminum oxide cluster structures have utilized HF, B3LYP, and MP2 methodologies with basis sets ranging from 6-31G* to 6-311+G-(3df).[26,30,31,32] The only hydration reaction mechanism modeled for aluminum oxide has been the embedded surface cluster modeling by Wittbrodt et al.[32] The geometries for clusters used for these embedded surface modeling computations were optimized at the HF/6-31+G* level of theory. Energies were then calculated at the B3LYP/6-311+G* and MP2/6-311+G* levels of theory using the HF/6-31+G* geometries. The goal of the computational work in this paper was to determine whether the computations could provide an explanation for the disparity in hydration kinetics. It was not clear whether there would be significant differences in geometries, energetics, and/or mechanisms between different levels of theory, which has been known to occur.[67] Therefore, the calculations on the AlO_2^- system were performed at five different levels of theory: HF/6-311+G(d(Al),p), B3LYP/6-31+G(d), B3LYP/6-311+G(2d,p), B3LYP/6-311+G(3d2f,2p), and MP2/6-311+G(2d,p). A comparison of the results revealed insignificant differences among the different levels of theory for the calculated geometries or reaction mechanisms. Detailed structural information for each structure, at all levels of theory, is available in Table 1S of the Supporting Information.

The overall reaction mechanism is provided in Figure 7, using the B3LYP/6-311+G(2d,p) level of theory. All levels of theory predict a linear geometry for AlO_2^- (structure **1A**). Initially, a hydrogen bond forms between O1 on AlO_2^- and H1 of the incoming H_2O (structure **2A)**. Second, a bond begins to form between Al and the water oxygen (O3) to form transition-state structure **TS3A**. The bond between oxygen (O3) and hydrogen (H1) on the water molecule then breaks, forming the trigonally coordinated $AlO_3H_2^-$ product (structure **4A**), which has two aluminol (AlOH) groups. This reaction is similar to hydrolysis of partially coordinated aluminum surface sites, which are known to form aluminol moieties.[17,18] Addition of the second water molecule proceeds in a similar manner with an initial H bond formed between a hydrogen atom of the incoming H_2O and the remaining unprotonated oxygen (O2) attached to Al (structure **5A**). Again, the transition state (**TS6A**) involves simultaneous Al−O bond formation and proton transfer as the oxygen (O4) of H_2O attacks the electrophilic Al atom and the O4−H3 bond begins to break. The final product ion, $AlO_4H_4^-$ (structure **7A**), has a tetrahedral geometry.

Energy values for the various structures, calculated at the different levels of theory, are summarized in Table 2. Figure 8a is a graphical representation of the energies summarized in Table 2 [the line for the B3LYP/6-311+G(3d2f,2p) level of

TABLE 2: Energetic Results from ab Initio Calculations[a]

$AlO_2^- + 2H_2O$	1A	2A	TS3A	4A	5A	TS6A	7A
B3LYP/6-31 G(d)	138.24	117.60	118.10	70.63	46.96	48.06	0
B3LYP/6-311+G(2d,p)	126.61	108.53	113.98	64.75	43.17	48.21	0
B3LYP/6-311+G(3d2f,2p)	128.00	110.25	115.48	65.24	44.08	48.82	0
MP2/6-311+G(2d,p)	128.42	110.67	116.10	66.93	45.48	50.55	0
MP2/6-311+G(d(Al),p)// HF/6-311+G(d(Al),p)	122.83	107.78	110.87	65.36	48.03	50.03	0
$Al_2O_4H^- + 2H_2O$	1B	2B	TS3B	4B	5B	TS6B	7B
B3LYP/6-311+G(2d,p)	119.60	99.98	103.21	51.75	33.21	34.51	0

[a] Relative energies (kcal/mol) are relative to the lowest-energy structure.

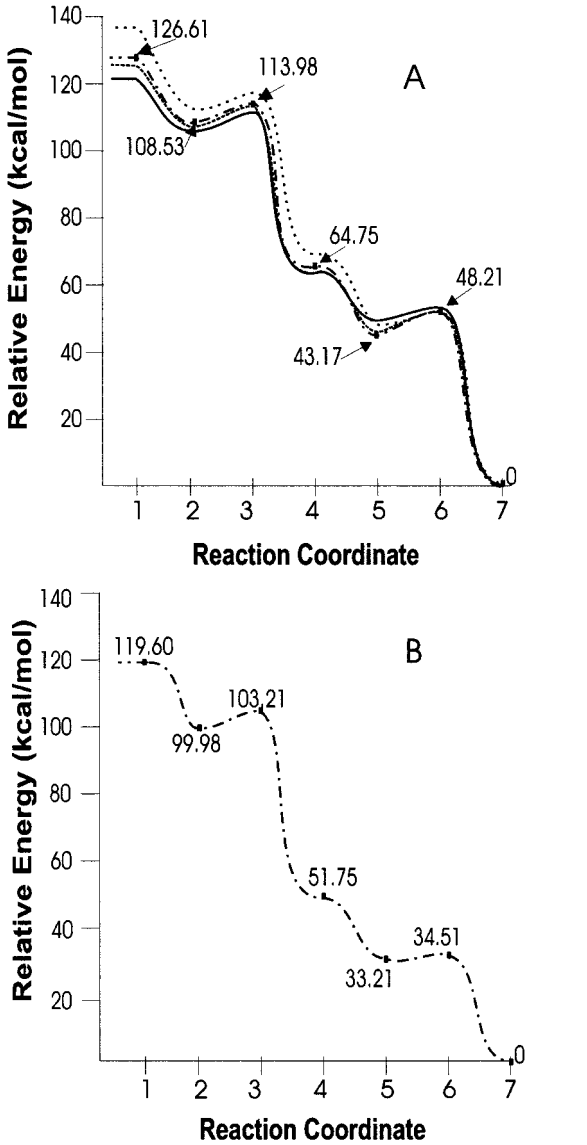

Figure 8. (A) Energy level diagram for $A1O_2^- + 2H_2O \rightarrow A1O_4H_4^-$. Legend: ———, MP2/6-311+G(dA1,p)//HF/6-311+G(d(A1),p); ·····, B3LYP/6-31+G(d); —·—·—, B3LYP/6-311+G(2d,p); and · · · ·, MP2/6-311+G(2d,p). (B) Energy level diagram for $A1_2O_4^- + 2H_2O \rightarrow A1_2O_6H_5^-$ utilizing B3LYP/6-311+G(2d,p) level of theory. Values for the B3LYP/6-311+G(2d,p) level of theory have been identified as reference points.

theory was omitted for clarity as it is essentially identical to the line for MP2/6-311+G(2d,p) level of theory]. From the plot in Figure 8a, it is obvious that the differences between various levels of theory are not as great for structures involved in the addition of the second H_2O molecule as they are for addition of the first H_2O molecule. The single-point MP2 energy calculations for HF/6-311+G(d(Al),p) geometries are generally higher than energies for the other levels of theory, whereas the MP2/6-311+G(2d,p) energies are generally lower. The energies calculated with the B3LYP/6-311+G(2d,p) level of theory are close to the overall average for all five energy calculation methods.

According to the B3LYP/6-311+G(2d,p) calculations (Figure 8a), the reaction between AlO_2^- and H_2O leading to formation of the intermediate **2A** (Figure 7) is barrierless, in the sense that the transition state is below the reactants. No potential energy well was found for an association between the oxygen on the water (O3) and the aluminum atom (Al). The energy barrier for formation of $AlO_3H_2^-$ (**4B**) is 5.5 kcal/mol, whereas the barrier for dissociation is 18.1 kcal/mol; therefore, **2A** isomerizes instead of dissociating. Similarly, the reaction of **4A** with H_2O results in formation of a hydrogen-bonded intermediate (**5A**). Again, no potential energy well was found for an attractive interaction between the aluminum atom (Al) and the oxygen of the incoming water (O4). The intermediate **5A** isomerizes because the energy barrier for dissociation is 21.6 kcal/mol, whereas the barrier for formation of $AlO_4H_4^-$ (**7A**) is merely 5 kcal/mol.

The molecular water adduct formation in the first step of the reaction mechanism leads to a molecular H_2O adsorption energy of 18 kcal/mol, which is approximately half that calculated by Wittbrodt et al.,[32] whose values range between 31 and 45 kcal/mol, depending on the model and level of theory employed. This discrepancy is not surprising because the molecular adsorption step in the hydration reaction modeled by Wittbrodt et al.[32] involves nucleophilic attack on an Al atom by the O atom of the water as opposed to H-bond formation between the water and a dangling O atom of AlO_2^- as in the current case. The surface model employed by Wittbrodt et al. only contained bridging O atoms. However, the 18 kcal/mol is only slightly outside the experimental range of 23−41 kcal/mol.[41] The energy barrier for formation of **TS3A** is 5.5 kcal/mol, as compared to 10−16 kcal/mol for transition-state barriers calculated by Wittbrodt et al. They also found that the products from chemisorption of one H_2O molecule are stablized by 45−60 kcal/mol, depending on the model used. This compares well with the 55 kcal/mol stabilization energy calculated for structure **4A**, $AlO_3H_2^-$, in this study. The second molecular water adduct, structure **5A**, gives a molecular adsorption energy of 22 kcal/mol, which is in good agreement with experimental values.[41] The energy barrier for **TS6A** is 5 kcal/mol, which is essentially the same as that for **TS3A**. The product, structure, **7A**, is 65 kcal/mol more stable than structure **4A**. The final product, structure, **7A**, is 127 kcal/mol more stable than the initial reactant, AlO_2^-. Wittbrodt et al.[32] also modeled adsorption of a second H_2O molecule for the cluster Al_8O_{12}. Depending on the theory used, they found that the product of the second water

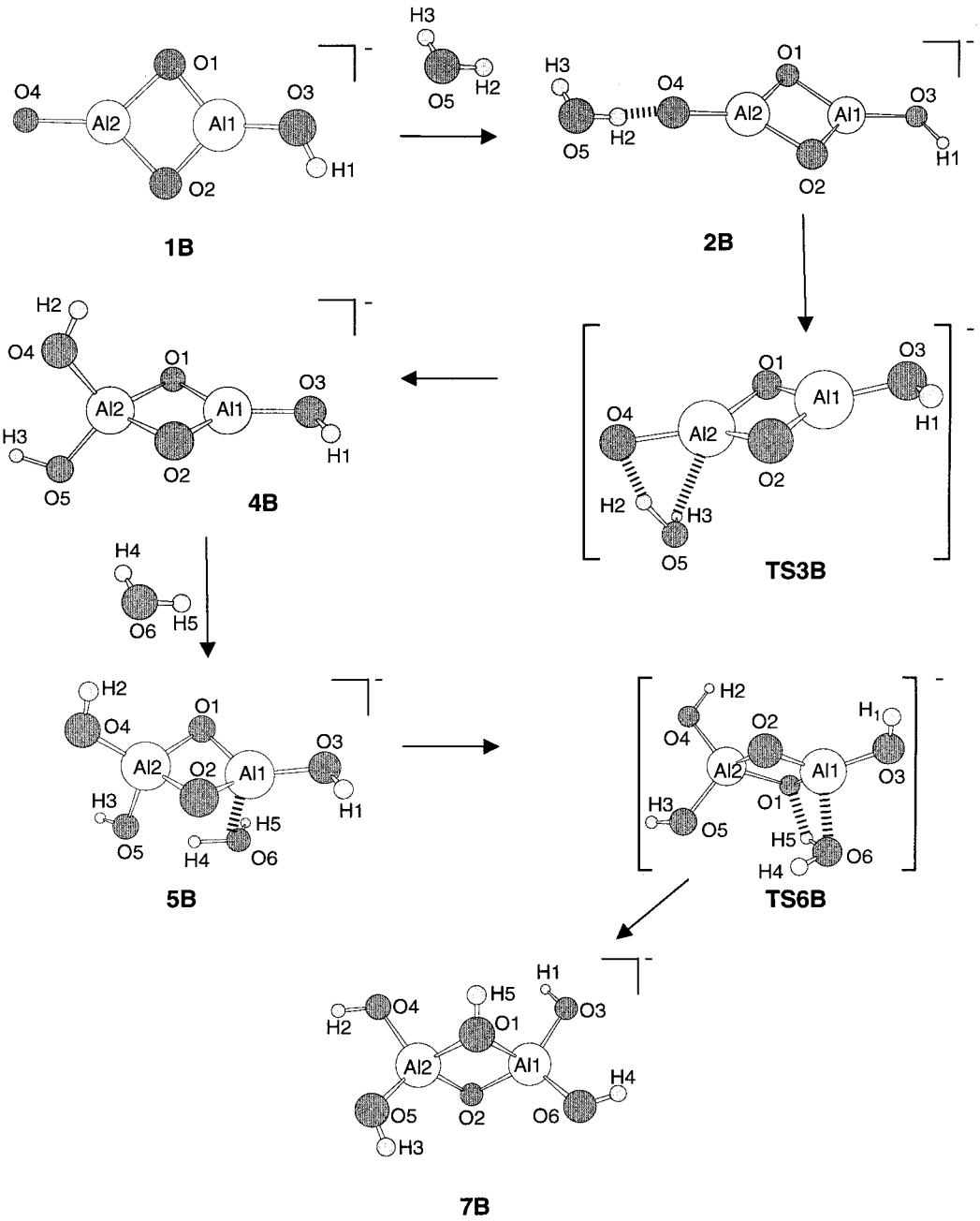

Figure 9. Reaction pathway for hydration of $A1_2O_4H^-$. Structures based on the B3LYP/6-311+G(2d,p) level of theory.

molecule was stabilized by 83−99 kcal/mol compared to the initial dehydrated reactant.

To confirm that the H_2O molecules have covalently bonded to AlO_2^-, as opposed to merely forming H-bonded adducts, CID experiments were performed to see if loss of H_2O would occur. In these experiments, the dihydrate species $AlO_2(H_2O)_2^-$ (*m*/*z* 95) was isolated. Subsequently, an axial RF pulse at the natural frequency of *m*/*z* 95 was applied to collisionally activate the anions. The RF pulse was applied with various combinations of time (10−500 ms) and amplitude (0.2−7.0 V_{p-p}). A maximum of 5% of the dehydrated species (*m*/*z* 59 and/or 77) was observed. As the RF amplitude was increased, a loss of signal at *m*/*z* 95 was observed, as ions were ejected from the IT-SIMS. In the IT-SIMS, H-bonded adducts normally require less than 0.1 V_{p-p} to dissociate (for a discussion of activation voltage vs dissociation energy in ion trap mass spectrometers, see Colorado and Brodbelt[68]). Because the dihydrated species $AlO_4H_4^-$ could not be fragmented, we conclude that it is a covalently bound species, which is consistent with the irreversible chemisorption observed in macroscopic hydration studies of alumina.[35]

$Al_2O_4H^-$ + $2H_2O$ → $Al_2O_6H_5^-$ Reaction Mechanism. Because a comparison of the results for the AlO_2^- system revealed insignificant differences between the different levels of theory for the calculated geometries or reaction mechanisms, the $Al_2O_4H^-$ system was investigated using the B3LYP/6-311+G(2d,p) level of theory. Energy values and structural details are summarized in Table 2 and Table 2S (of the Supporting Information), respectively.

Figure 9 shows the overall hydration mechanism using the B3LYP/6-311+G(2d,p) level of theory. In general, the hydration mechanism for addition of the first H_2O is similar to the hydration mechanisms in Figure 7 for AlO_2^-. As seen in structure **1B**, the initial reactant, $Al_2O_4H^-$, has the expected rhombus-like core,[26,28,31] similar to that of Al_2O_4 in Figure 1. The mechanism for the addition of the first H_2O involves

formation of a hydrogen bond between a hydrogen atom of the incoming water (H2) and the dangling oxygen (O4) of $Al_2O_4H^-$ (**1B**), leading to the molecular water adduct in structure **2B**. No attractive interaction was observed between O5 of the incoming H_2O and the aluminum atoms (Al1 or Al2). In the transition-state structure, **TS3B**, the water molecule oxygen (O5) attacks the electrophilic Al2, while the bond between the water oxygen (O5) and hydrogen (H2) begins to break. The hydrogen-bonded intermediate, **2B**, isomerizes to form $Al_2O_5H_3^-$ (**4B**) because the energy barrier for formation of **4B** is only 3.2 kcal/mol, whereas the reverse dissociation barrier is 19.6 kcal/mol.

As illustrated in Figure 9, addition of H_2O to $Al_2O_5H_3^-$ occurs by a different mechanism than does water addition to AlO_2^-, $AlO_3H_2^-$, and $Al_2O_4H^-$. In this case, there is an attractive interaction between the oxygen atom (O6) and the aluminum atom (Al1) of $Al_2O_5H_3^-$. Unlike the mechanism for AlO_2^-, $AlO_3H_2^-$, and $Al_2O_4H^-$, no hydrogen-bonded adduct is formed as an intermediate because there is no electron-density-rich dangling O atom available. Instead, there is a nucleophilic attack on the trigonally coordinated aluminum (Al1) by the O6 of the incoming H_2O to form structure **5B** (Figure 9). Aside from the association between Al1 and O6, transition state **TS6B** also has an association between H5 of the H_2O and one of the bridging oxygens (O1). In the final product, $Al_2O_6H_5^-$ (structure **7B)**, both Al atoms have two aluminol groups and are bridged together by two oxygen atoms. Although one of the bridging oxygen atoms is protonated (O1−H5), it still appears to be bridging the two Al atoms. The bond lengths between the Al atoms and the protonated oxygen of the bridging group (O1H5) are ∼1.9 Å, as compared to ∼1.75 Å for the bond lengths between the Al atoms and the unprotonated bridging oxygen (O2) atom. Calculations by Wittbrodt et al.[32] resulted in similar protonation of bridging O atoms.

CID experiments were also performed on the dihydrate $Al_2O_4H(H_2O)_2^-$ species to confirm that water was covalently bound. First, the dihydrate species $Al_2O_4H(H_2O)_2^-$ (*m*/*z* 155) was isolated. Second, an axial RF pulse at the natural frequency of *m*/*z* 155 was applied with various combinations of time (10−500 ms) and amplitude (0.2−7.0 V_{p-p}) to collisionally activate the anions. No dehydrated species (*m*/*z* 119 and/or 137) were observed. Only loss of signal at *m*/*z* 155 was observed as ions were ejected from the IT-SIMS as the RF amplitude increased. Aside from the loss of H_2O, fragmentation of the dihydrated dimer species, $Al_2O_4H(H_2O)_2^-$, could have occurred, but was not observed. Dissociation of the core structure of the dimer (Al_2O_4) is not expected because the estimated dissociation energy is 180 kcal/mol for the rhombus-like geometry.[26]

Table 2 contains the energy values calculated for each structure in Figure 9. As indicated by the B3LYP/6-311+G(2d,p) energy values illustrated in Figure 8b, the molecular H_2O adsorption energy for addition of the first water to form structure **2B** (Figure 9) is only 10 kcal/mol, which is half that for either of the molecular water adducts formed during hydration of AlO_2^-. The energy barrier for formation of **TS3B** is 3 kcal/mol, which is also approximately half the transition-state barrier for either hydration step of AlO_2^-. The stabilization energy for formation of structure **4B** is 78 kcal/mol. This value is slightly greater than either the 45−60 kcal/mol stabilization energy range calculated by Wittbrodt et al.[32] or the values obtained for the hydration steps for AlO_2^-. Although the mechanism for the second hydration step depicted in Figure 9 is slightly different from that of the first hydration step, it is similar to the hydration mechanisms predicted by Wittbrodt et al. for alumina clusters without dangling oxygen atoms. However, the molecular adsorption energy of 19 kcal/mol for formation of structure **5B** is still low compared to the values reported by Wittbrodt et al., but is close to reported experimental values.[41] The energy barrier for formation of **TS6B** is a mere 1.3 kcal/mol, which is only ∼10% as large as values reported by Wittbrodt et al. The stabilization energy between structures **7B** and **4B** is 52 kcal/mol and compares well with values by Wittbrodt et al. The overall stabilization energy for the dihydration of $Al_2O_4H^-$ is 120 kcal/mol, which is close to that of AlO_2^- (127 kcal/mol).[41]

Even though the reactions occur by similar mechanisms, the hydration rate constants vary by orders of magnitude. In particular, $Al_2O_4H^- + H_2O \rightarrow Al_2O_5H_3^-$ (eq 6) is the fastest with a rate constant of 2×10^{-9} cm^3 molecule^{-1} s^{-1}, while $AlO_2^- + H_2O \rightarrow AlO_3H_2^-$ (eq 1) is the slowest with a rate constant of 4×10^{-11} cm^3 molecule^{-1} s^{-1}. The only reaction that occurs by a slightly different mechanism is the second hydration step for $Al_2O_4H^-$ (eq 7), which is initiated by nucleophilic attack of H_2O on an aluminum atom. Presumably, this mechanism occurs because there are no unprotonated dangling oxygens present; however, it is not certain that nucleophilic attack of H_2O on Al would not occur in the presence of dangling oxygens on other $Al_xO_y^-$ clusters. The reaction $Al_2O_5H_3^- + H_2O \rightarrow Al_2O_6H_5^-$ (eq 7) occurs with an intermediate rate constant of 8×10^{-10} cm^3 molecule^{-1} s^{-1}, but has the lowest TS barrier (1.3 kcal/mol). It does not appear that the disparity between observed rate constants can be explained by differences in reaction mechanisms or energetics.

Neither the calculated mechanisms nor ADO theory[62,63,64] adequately accounts for the disparity in observed rate constants. However, the structures of the aluminum oxide anion cluster do suggest a rather simplistic explanation. An examination of the magnetic dipoles of the reactants, for each hydration step, reveals an interesting trend. The reactants have the following dipole moments: 0 D (AlO_2^-), 2.74 D ($AlO_3H_2^-$), 3.41 D ($Al_2O_5H_3^-$), and 9.27 D ($Al_2O_4H^-$). The trend in increasing dipole moment follows the trend in increasing rate constants: $4 \times 10^{-11} < 4 \times 10^{-10} < 8 \times 10^{-10} < 2 \times 10^{-9}$ cm^3 molecule^{-1} s^{-1}. The correlation of the rate constants with the dipole moment of the cluster anions would explain the failure of ADO theory to predict different rate constants for the reactions. ADO theory for ion/molecule reactions takes into account the dipole moment of the molecule and the charge of the ion. However, the charge distribution on the ion is not accounted for by the ADO calculations. For large polar ions, the charge distribution may affect the reaction rate by directing the incoming polar molecule to the reaction site. For example, AlO_2^- has no dipole moment, and the reaction is slow because the water molecules are not being preferentially oriented. However, once AlO_2^- is hydrated to form $AlO_3H_2^-$ (structure **4A**, Figure 7), the dipole moment is 2.74 D. This ion then reacts faster because the incoming H_2O is preoriented such that one of its electropositive hydrogen atoms is directed toward the electron-rich dangling oxygen of $AlO_3H_2^-$. The behavior of $Al_2O_4H^-$ is also consistent with this explanation. Hydration initially occurs very rapidly because the very uneven charge distribution (9.27 D) extends further into space to orient and attract H_2O molecules to the reactive site. After reacting with one water molecule to form $Al_2O_5H_3^-$ (structure **4B**, Figure 9), the dipole moment is reduced to 3.41 D. The subsequent hydration reaction proceeds more slowly because the less concentrated charge does not extend as far and, therefore, does not attract and preorient H_2O molecules as effectively. The dipole moment of the ion provides a quick and simple way of

TABLE 3: Mulliken Charge Values for Selected Structures in Figures 7 and 9

atom	AlO_2^- (**1A**)	$AlO_3H_2^-$ (**4A**)	$Al_2O_4H^-$ (**1B**)	$Al_2O_5H_3^-$ (**4B**)
Al1	0.79	1.20	1.17	0.97
Al2	NA	NA	0.99	1.86
O1	−0.89	−0.83	−0.87	−0.96
O2	−0.89	−1.01	−0.86	−0.93
O3	NA	−0.83	−0.73	−0.75
O4	NA	NA	−0.95	−0.95
O5	NA	NA	NA	−0.97
H1	NA	0.24	0.26	0.25
H2	NA	0.24	NA	0.23
H3	NA	NA	NA	0.25
sum	−1.00	−1.00	−1.00	−1.00

accounting for the effect that electron distribution in large ions has on reaction rates.

Further insight can be gained by evaluating the Mulliken charge distributions for the four reactants AlO_2^-, $AlO_3H_2^-$, $Al_2O_4H^-$, and $Al_2O_5H_3^-$. The Mulliken charge values are summarized in Table 3. Although AlO_2^- has a dipole moment of 0 D, the oxygen atoms (O1 and O2) have a net −0.8 charge, which would assist in orienting the incoming water molecule. The reactive oxygen (O2) in $AlO_3H_2^-$ has a net charge of −1.0, which is slightly more negative than the oxygen atoms in AlO_2^-, and $AlO_3H_2^-$ has a greater rate constant for hydration than does AlO_2^-. Based on the −0.95 charge on O4 of $Al_2O_4H^-$, the predicted rate constant would be less than that for $AlO_3H_2^-$, but greater than that for AlO_2^-. However, the correlation between the individual negative potentials on the reactive oxygens and the rate constants breaks down in the case of $Al_2O_4H^-$ because the rate constant for $Al_2O_4H^-$ is an order of magnitude greater than that for $AlO_3H_2^-$. In the case of $Al_2O_5H_3^-$, the interaction with H_2O is different because the oxygen atom of the water (O6) attacks one of the aluminum atoms (Al1). One might expect that the difference in reaction mechanisms might be related to the positive potential on the aluminum atom(s). However, the charge on Al1 in $Al_2O_5H_3^-$ is 1.0 as compared to charges of 1.0, 1.2, and 0.8 for aluminum atoms on the other anions, which react via the hydrogen-bonded adduct. Therefore, the absence or presence of a dangling O atom still appears to be the primary factor determining which reaction mechanism is followed.

IV. Conclusion

In the gas-phase environment of the IT-SIMS, AlO_2^- and $Al_2O_4H^-$ both react by consecutively adding two H_2O molecules. As indicated by ab initio calculations, these gas-phase hydration reactions occur by a dissociative mechanism similar to that expected for alumina surfaces. The ab initio calculations revealed that a four-membered transition state, involving simultaneous Al−O bond formation and proton transfer, is formed for all of the observed hydration reactions. For three of the reactions, a hydrogen bond is initially formed between water and a dangling oxygen atom of the anion, and the transition-state barriers for these three reactions were also similar (3−5.5 kcal/mol). However, for addition of the second water in the $Al_2O_4H^-$ system, the reaction was initiated by nucleophilic attack on an aluminum atom by the water oxygen atom because a dangling oxygen was not present. For this reaction, a significant later transition was observed, with respect to the Al−O and H−O bond lengths. The transition-state barrier for this reaction was 1.3 kcal/mol. Although the reaction mechanisms and thermodynamics are similar, the rate constants vary over 2 orders of magnitude (10^{-11}−10^{-9} cm^3 molecule^{-1} s^{-1}). The widely disparate reaction rates cannot be explained solely by differences in reaction mechanism or thermodynamics. However, the reactivity differences do correlate with the dipole moments of the aluminum oxide anions (rate constants increase with increasing dipole of the reactant anion), which may serve to preorient the incoming water molecule.

The ReO_4^- particle beam of the IT-SIMS allows anions to be sputtered off of the alumina surface and into the gas phase. In the gas phase, the individual anion types are readily accessible for kinetic studies. This is in contrast to surface kinetic studies, which are often an average over multiple types of sites. Future studies on larger oligomer species may help elucidate how well gas-phase reactions correlate with surface reactions.

Acknowledgment. The authors thank Anthony D. Appelhans for assistance with instrumentation and Glen F. Kessinger for computational assistance and helpful discussions concerning alumina chemistry. All DFT and MP2/6-311+G(2d,p) calculations were supported in part by a grant of HPC time from the Department of Defense HPC Center at Aberdeen Proving Grounds, MD. The authors gratefully acknowledge the funding support of the Environmental Systems Research and Analysis Program, United States Department of Energy, Contract DE-AC-07-99ID13727 BBWI.

Supporting Information Available: Tables 1S and 2S contain structural results from ab initio calculations for the hydration reactions $AlO_2^- + 2H_2O \rightarrow AlO_4H_4^-$ and $Al_2O_4H^- + 2H_2O \rightarrow Al_2O_6H_5^-$, respectively. This material is available free of charge via the Internet at http://pubs.acs.org.

References and Notes

(1) Mackrodt, W. C. *J. Chem. Soc., Faraday Trans. 2* **1989**, *85*, 541.
(2) Tasker, P. W. *Adv. Ceram.* **1988**, *10*, 176.
(3) Johnson, M. A.; Stefanovich, E. V.; Truong, T. N. *J. Phys. Chem. B* **1998**, *102*, 6391.
(4) Johnson, M. A.; Stefanovich, E. V.; Truong, T. N. *J. Phys. Chem. B* **1999**, *103*, 3391.
(5) Salasco, L.; Dovesi, R.; Orlando, R.; Causa, M. *Mol. Phys.* **1991**, *72*, 267.
(6) Stefanovich, E. V.; Truong, T. N. *Chem. Phys. Lett.* **1999**, *299*, 623.
(7) Puchin, V. E.; Stefanovich, E. V.; Truong, T. N. *Chem. Phys. Lett.* **1999**, *304*, 258.
(8) Schroeder, D.; Schwarz, H. *Angew. Chem., Int. Ed. Engl.* **1995**, *34*, 1973.
(9) Gustev, G. L.; Khanna, S. N.; Rao, B. K.; Jena, P. *J. Phys. Chem. A* **1999**, *103*, 5812.
(10) Guo, B. C.; Kerns, K. P.; Castleman, A. W. J. *J. Mass Spectrom.* **1992**, *117*, 129.
(11) Bell, R. C.; Zemski, K. A.; Kerns, K. P.; Deng, H. T.; Castleman, A. W. J. *J. Phys. Chem. A* **1998**, *102*, 1733.
(12) Fisher, K. J.; Dance, I. G.; Willett, G. D. *Rapid Commun. Mass Spectrom.* **1996**, *10*, 106.
(13) Johnston, R. L. *Philos. Trans. R. Soc. London, A* **1998**, *356*, 211.
(14) Jortner, J. *Z. Phys. D* **1992**, *24*, 247.
(15) Fialko, E. F.; Kikhtenko, A. V.; Goncharov, V. B.; Zamaraev, K. I. *J. Phys. Chem. B* **1997**, *101*, 5772.
(16) Deng, H. T.; Kerns, K. P.; Castleman, A. W. J. *J. Phys. Chem.* **1996**, *100*, 13386.
(17) White, G. N.; Zelany, L. W. *Clays Clay Miner.* **1988**, *36*, 141.
(18) Zachara, J. M.; McKinley, J. P. *Aquat. Sci.* **1993**, *55*, 250.
(19) Rosenwaks, S.; Steele, R. E.; Broida, H. P. *J. Chem. Phys.* **1975**, *63*, 1963.
(20) Hebert, T.; Schriever, U.; Kolb, D. M. *Chem. Phys. Lett.* **1992**, *200*, 258.
(21) Dagdigian, P. J.; Cruse, H. W.; Zare, R. N. *J. Chem. Phys.* **1975**, *62*, 1824.
(22) Sayers, M. J.; Gole, J. L. *J. Chem. Phys.* **1977**, *67*, 5442.
(23) Kasatani, K.; Higashide, H.; Shinohara, H.; Sato, H. *Chem. Phys. Lett.* **1990**, *174*, 71.
(24) Zenouda, C.; Blottiau, P.; Chambaud, G.; Rosmus, P. *J. Mol. Struct.* **1999**, *458*, 61.

(25) Andrews, L.; Burkholder, T. R.; Yustein, J. T. *J. Phys. Chem.* **1992**, *96*, 10182.
(26) Archibong, E. F.; St-Amant, A. *J. Phys. Chem. A* **1998**, *102*, 6877.
(27) Serebrennikov, L. V.; Osin, S. B.; Maltsev, A. A. *J. Mol. Struct.* **1982**, *81*, 25.
(28) Archibong, E. F.; St-Amant, A. *J. Phys. Chem. A* **1999**, *103*, 1109.
(29) Wu, H.; Li, X.; Wang, X.-B.; Ding, C.-F.; Wang, L.-S. *J. Chem. Phys*. **1998**, *109*, 449.
(30) Nemukhin, A. V.; Weinhold, F. *J. Chem. Phys.* **1992**, *97*, 3420.
(31) Desai, S. R.; Wu, H.; Rohlfing, C. M.; Wang, L.-S. *J. Chem. Phys.* **1997**, *106*, 1309.
(32) Wittbrodt, J. M.; Hase, W. L.; Schlegel, H. B. *J. Phys. Chem. B* **1998**, *102*, 6539.
(33) Desai, R.; Hussain, M.; Ruthven, D. M. *Can. J. Chem. Eng.* **1992**, *70*, 699.
(34) McHale, J. M.; Navrotsky, A.; Perrotta, A. J. *J. Phys. Chem. B* **1997**, *101*, 603.
(35) Kotoh, K.; Enoda, M.; Matsui, T.; Nishikawa, M. *J. Chem. Eng. Jpn.* **1993**, *26*, 355.
(36) Kotoh, K.; Enoda, M.; Matsui, T.; Nishikawa, M. *J. Chem. Eng. Jpn.* **1993**, *26*, 570.
(37) Coustet, V.; Jupille, J. *Surf. Interface Anal.* **1994**, *22*, 280.
(38) Morrow, B. A. *Stud. Surf. Sci. Catal.* **1990**, *57*, A161.
(39) Knözinger, H.; Ratnasamy, P. *Catal. Rev.*−*Sci. Eng.* **1978**, *17*, 31.
(40) Elam, J. W.; Nelson, C. E.; Cameron, M. A.; Tolbert, M. A.; George, S. M. *J. Phys. Chem. B* **1998**, *102*, 7088.
(41) Nelson, C. E.; Elam, J. W.; Cameron, M. A.; Tolbert, M. A.; George, S. M. *Surf. Sci.* **1998**, *416*, 341.
(42) Groenewold, G. S.; Appelhans, A. D.; Ingram, J. C. *J. Am. Soc. Mass Spectrom.* **1998**, *9*, 35.
(43) Appelhans, A. D.; Groenewold, G. S.; Ingram, J. C.; Delmore, J. E.; Dahl, D. A. In *Secondary Ion Mass Spectrometry SIMS X*; Bennighoven, A., Hagenoff, B., Werner, H. W., Eds.; Wiley: New York, 1997; p 935.
(44) Groenewold, G. S.; Appelhans, A. D.; Ingram, J. C.; Gresham, G. L.; Gianotto, A. K. *Talanta* **1998**, *47*, 981.
(45) Ingram, J. C.; Groenewold, G. S.; Appelhans, A. D.; Dahl, D. A.; Delmore, J. E. *Anal. Chem*. **1996**, *68*, 1309.
(46) Ingram, J. C.; Appelhans, A. D.; Groenewold, G. S. *Int. J. Mass Spectrom. Ion Processes* **1998**, *175*, 253.
(47) Delmore, J. E.; Appelhans, A. D.; Peterson, E. S. *Int. J. Mass Spectrom. Ion Processes* **1995**, *146/147*, 15.
(48) Delmore, J. E.; Appelhans, A. D.; Peterson, E. S. *Int. J. Mass Spectrom. Ion Processes* **1991**, *108*, 179.
(49) Groenewold, G. S.; Delmore, J. E.; Olson, J. E.; Appelhans, A. D.; Ingram, J. C.; Dahl, D. A. *Int. J. Mass Spectrom. Ion Processes* **1997**, *163*, 185.
(50) Bartmess, J. E.; Georgiadis, R. M. *Vacuum* **1983**, *33*, 149.
(51) Todd, J. F. J. In *Practical Aspects of Ion Trap Mass Spectrometry*; March, R. E., Todd, J. F. J., Eds.; CRC Press: New York, 1995; Vol. I, p 4.
(52) Schmidt, M. W.; Baldridge, K. K.; Boatz, J. A.; Jensen, J. H.; Koseki, S.; Matsunaga, N.; Gordon, M. S.; Nguyen, K. A.; Su, S.; Windus, T. L.; Elbert, S. T.; Montgomery, J.; Dupuis, M. *J. Comput. Chem.* **1993**, *14*, 1347.
(53) Gonzalez, C.; Schlegel, H. B. *J. Chem. Phys*. **1989**, *90*, 2154.
(54) Gonzalez, C.; Schlegel, H. B. *J. Phys. Chem.* **1990**, *94*, 5523.
(55) Møller, C.; Plesset, M. S. *Phys. Rev.* **1934**, *46*, 618.
(56) Krishnan, R.; Frisch, M. J.; Pople, J. A. *J. Chem. Phys.* **1980**, *72*, 4244.
(57) Frisch, M. J.; Trucks, G. W.; Schlegel, H. B.; Scuseria, G. E.; Robb, M. A.; Cheeseman, J. R.; Zakrzewski, V. G.; Montgomery, J. A., Jr.; Stratmann, R. E.; Burant, J. C.; Dapprich, S.; Millam, J. M.; Daniels, A. D.; Kudin, K. N.; Strain, M. C.; Farkas, O.; Tomasi, J.; Barone, V.; Cossi, M.; Cammi, R.; Mennucci, B.; Pomelli, C.; Adamo, C.; Clifford, S.; Ochterski, J.; Petersson, G. A.; Ayala, P. Y.; Cui, Q.; Morokuma, K.; Malick, D. K.; Rabuck, A. D.; Raghavachari, K.; Foresman, J. B.; Cioslowski, J.; Ortiz, J. V.; Stefanov, B. B.; Liu, G.; Liashenko, A.; Piskorz, P.; Komaromi, I.; Gomperts, R.; Martin, R. L.; Fox, D. J.; Keith, T.; Al-Laham, M. A.; Peng, C. Y.; Nanayakkara, A.; Gonzalez, C.; Challacombe, M.; Gill, P. M. W.; Johnson, B.; Chen, W.; Wong, M. W.; Andres, J. L.; Head-Gordon, M.; Replogle, E. S.; Pople, J. A.; *Gaussion 98*, revision A.4; Gaussian, Inc.: Pittsburgh, PA, 1998.
(58) Becke, A. D. *J. Chem. Phys.* **1993**, *98*, 5648.
(59) Lee, C.; Yang, W.; Parr, R. *Phys. Rev. B* **1988**, *37*, 785.
(60) Peng, C. *Isr. J. Chem.* **1994**, *33*, 449.
(61) Peng, C. *J. Comput. Chem.* **1996**, *17*, 49.
(62) Su, T.; Bowers, M. T. *Int. J. Mass Spectrom. Ion Phys.* **1973**, *12*, 347.
(63) Su, T.; Bowers, M. T. *J. Chem. Phys.* **1973**, *58*, 3027.
(64) Su, T.; Bowers, M. T. *Int. J. Mass Spectrom. Ion Phys.* **1975**, *17*, 211.
(65) Benson, S. W. *The Foundation of Chemical Kinetics*; McGraw-Hill: New York, 1960.
(66) Moore, J. W.; Pearson, R. G. *Kinetics and Mechanism*, 3rd ed.; John Wiley: New York, 1981.
(67) Tomlinson, M. J.; Scott, J. R.; Wilkins, C. L.; Wright, J. B.; White, W. E. *J. Mass Spectrom.* **1999**, *34*, 958.
(68) Colorado, A.; Brodbelt, J. *J. Am. Soc. Mass Spectrom.* **1996**, *7*, 1116.